Modelling for the Tensile Fracture Characteristic of Cellular Structures under Tensile Load with Size Effect

Yan Wu, Li Yang
Department of Industrial Engineering, University of Louisville, Louisville, KY 40292

Abstract

In the unit cell-based design of cellular structures, an important issue is the effect of the cellular pattern size (i.e. the number of unit cell numbers along different orientations) on their mechanical properties. Among these properties, the fracture properties are of great importance for a broad range of applications but have been rarely investigated. In this work the size effects on the fracture characteristic (including failure initiation, crack propagation and failure patterns) of the BCC, octet-truss, auxetic and octahedral structures under tensile loadings were analyzed based analytical models. It was found that for the fracture of the cellular structures there exist significant coupling effects between the unit cell topology and the cellular pattern size. The results also clearly suggested the importance of dedicating more design attentions to the boundaries of the cellular structures during their fracture designs. This study provides additional insights into the design considerations for the fracture properties of the cellular structures.

Keywords: Tensile Fracture, Cellular Structures, Crack propagation, Size effect

1. Introduction

The cellular solid is made up of an interconnected network of solid struts or plates which form the edges and faces of cells. These cellular solids give rise to a unique combination of properties which are exploited in engineering design: their low weights make them attractive for structural sandwich panels, their ability to undergo large deformations at relatively low stresses makes them ideal for absorbing the energy of impacts, their low thermal conductivity makes them excellent insulators, and their high specific surface areas make them attractive for substrates for catalysts for chemical reactions [1-6]. The cellular solid, usually with infinite unit cells, is treated more like a material rather than a structure. For such cellular solids, the generic equations or discussions regarding the behavior are commonly modelled using the ideal periodic boundary conditions. However, as finite-size cellular structures often exhibit mechanical properties that are significantly influenced by the size effects, the observations and conclusions of the cellular characteristics based on infinite cellular solids are not representative under these design scenarios. Ozdemir et al. [7, 8] investigated the crushing behavior of various cellular structures including cubic, diamond, and re-entrant cube with different numbers of layers through finite element simulations and experiments. Their results showed that the compression modulus and initial yield stress are dependent on the number of layers due to the influence of weaker boundary conditions on the internal layers. Li et al. [9] discussed the influence of different applied boundary conditions on the compressive characteristics of BCC lattice patterns. They found that the introduction of full constraint at both top and bottom surfaces resulted in an increase of elastic modulus by 1.5 times compared to the unconstrained conditions, indicating that the mechanical properties calculated from the isolated cellular cores

cannot be directly extrapolated to predict the properties of the sandwich panel. Yang [10] investigated both lateral and along-the-stress size effects of multiple cellular structural designs under compressive stress using simulations. However, size effects on the failure characteristics of cellular structures have not been explored adequately.

In this paper, an analytical model was established to model the tensile failure behavior of the finite-size 3D cellular structures. The effects of unit cell numbers on the deformation behaviors and failure mechanism were systematically studied, including Young's modulus, tensile strength, energy absorption and failure pattern. A comparison of these properties among different designs (BCC, octet-truss, auxetic and octahedral structures) is provided to evaluate their potentials in structural applications.

2. Unit Cell Design

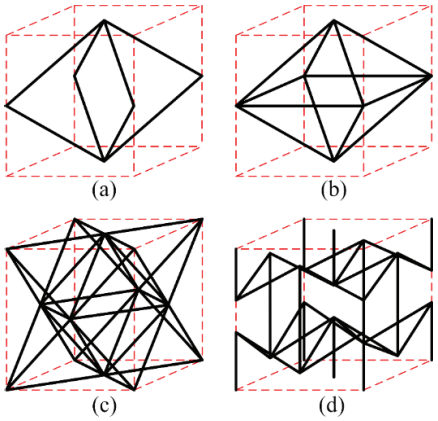

Fig. 1 (a) BCC; (b) Octahedral; (c) Octet-truss; (d) Auxetic

In this study, Body Centered Cubic (BCC), Octahedral, Octet-truss and Auxetic structures are used as the basic unit cells shown in Fig.1. All four cellular designs have been designed and realized via additive manufacturing and widely studied for mechanical properties. These cellular designs were selected to investigate the potential relationship between size effects and tensile fracture properties. Among these designs, the auxetic structure exhibits negative Poisson's ratios, the octet-truss structure exhibits high modulus and stretch-dominated deformation, while the BCC lattice and octahedral structures both exhibit bending-dominated deformation. In Fig.1, the size of the red cube was set as 12mm×12mm×12mm, which defines the bounding volume of the cellular unit cells. The diameter of struts was set as 1 mm for all the structures. For the BCC structure (relative density of 4.44%) in Fig. 1(a), the strut length was set as 10mm. For the octahedral structure (relative density of 8.45%) in Fig. 1(b), the oblique strut length was set as 10mm and the horizontal strut length was set as 14mm. For the octet-truss structure (relative density of 15.62%) in Fig. 1(c), the strut length was set as 8mm. For the auxetic structure (relative density of 12.78%) in Fig. 1(d), the opening angle was set as 60degree, the re-entrant strut length was set as 6.7mm and the vertical strut length was set as 9.1mm. For all of these structures, the unit cell numbers vary from 2x2x2 to 8x8x8. Ti-6Al-4V was arbitrarily selected as the material in the analytical calculation with the Young's modulus

of 114GPa, the shear modulus of 43GPa, and the yield strength of 1050MPa. As the study was not intended to investigate material effects, no further treatment was implemented to the material property setting, and a simple perfectly elastic material model was assumed.

3. Matrix displacement method for fracture properties modeling

3.1 Matrix displacement method for lattice structures

The cellular structures are considered as networks of interconnected struts or walls with porosities. Each strut or wall is considered to be rigidly connected at the nodes. Therefore, without losing generality, a 3D Timoshenko beam problem was considered. A 3D beam element is a structural member generally subjected to transverse loading, axial loading, bending moment and torsional moment, shown in Fig. 2. In Fig. 2, the beam is of length L with axial local coordinate x and transverse local coordinate y and z. The local transverse nodal displacements are given by v_i and w_i and the rotations by θ_{iy} and θ_{iz}. The local axial nodal displacements are given by u_i and the rotations by θ_{ix}. The local nodal transverse forces are given by F_{iy} and F_{iz}. The local nodal axial forces are given by F_{ix}. The local nodal bending moments are given by M_{iy} and M_{iz}. And the local nodal torsional moments are given by M_{ix}.

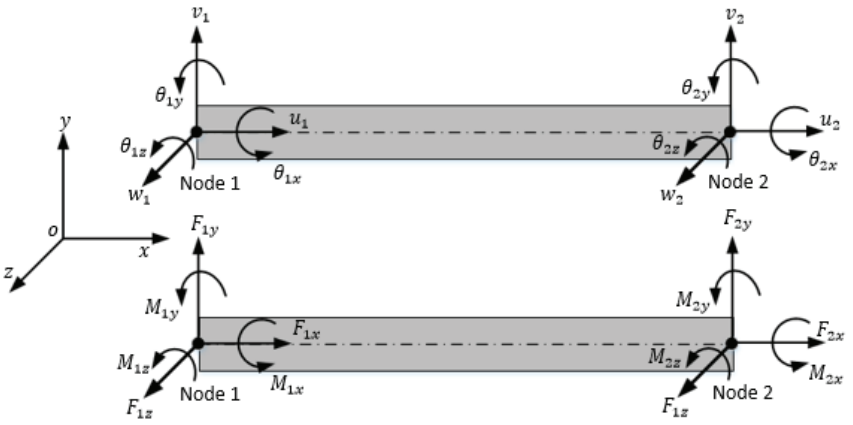

Fig. 2 3D Beam element with nodal displacement and nodal loadings

Under the local coordinate system (*xoy*), the forces at the ends of a beam element are related to the corresponding displacements at the ends by the element stiffness matrix, i.e.,

$$\begin{Bmatrix} {F_i}^e \\ {F_j}^e \end{Bmatrix} = [\mathrm{K}]^e \begin{Bmatrix} {d_i}^e \\ {d_j}^e \end{Bmatrix} \tag{1}$$

where ${d_i}^e$ and ${d_j}^e$ are the displacement vectors at node *i* and *j* respectively, and ${F_i}^e$ and ${F_j}^e$ are force vectors at node *i* and *j* respectively for the element *ij*. The element stiffness matrix $[\mathrm{K}]^e$ for a single 3D beam element is shown in Eq. (2). E, G, A, *L* and I are Young's modulus, shear modulus, area of the cross section, length of the strut and the second moment of inertia, respectively. $[\mathrm{K}]^e$ is only decided by the structure and material and has no dependency on the applied forces.

$$[K] = \begin{bmatrix}
\frac{EA}{L} & 0 & 0 & 0 & 0 & 0 & -\frac{EA}{L} & 0 & 0 & 0 & 0 & 0 \\
0 & \frac{12EI_z}{L^3(1+\varphi_y)} & 0 & 0 & \frac{6EI_z}{L^2(1+\varphi_y)} & 0 & 0 & -\frac{12EI_z}{L^3(1+\varphi_y)} & 0 & 0 & \frac{6EI_z}{L^2(1+\varphi_y)} & 0 \\
0 & 0 & \frac{12EI_y}{L^3(1+\varphi_z)} & 0 & 0 & \frac{6EI_y}{L^2(1+\varphi_z)} & 0 & 0 & -\frac{12EI_y}{L^3(1+\varphi_z)} & 0 & 0 & \frac{6EI_y}{L^2(1+\varphi_z)} \\
0 & 0 & 0 & \frac{GJ}{L} & 0 & 0 & 0 & 0 & 0 & -\frac{GJ}{L} & 0 & 0 \\
0 & \frac{6EI_z}{L^2(1+\varphi_y)} & 0 & 0 & \frac{(4+\varphi_y)EI_z}{L(1+\varphi_y)} & 0 & 0 & -\frac{6EI_z}{L^2(1+\varphi_y)} & 0 & 0 & \frac{(2-\varphi_y)EI_z}{L^2(1+\varphi_y)} & 0 \\
0 & 0 & \frac{6EI_y}{L^2(1+\varphi_z)} & 0 & 0 & \frac{(4+\varphi_z)EI_y}{L(1+\varphi_z)} & 0 & 0 & -\frac{6EI_y}{L^2(1+\varphi_z)} & 0 & 0 & \frac{(2-\varphi_z)EI_y}{L^2(1+\varphi_z)} \\
-\frac{EA}{L} & 0 & 0 & 0 & 0 & 0 & \frac{EA}{L} & 0 & 0 & 0 & 0 & 0 \\
0 & -\frac{12EI_z}{L^3(1+\varphi_y)} & 0 & 0 & -\frac{6EI_z}{L^2(1+\varphi_y)} & 0 & 0 & \frac{12EI_z}{L^3(1+\varphi_y)} & 0 & 0 & -\frac{6EI_z}{L^2(1+\varphi_y)} & 0 \\
0 & 0 & -\frac{12EI_y}{L^3(1+\varphi_z)} & 0 & 0 & -\frac{6EI_y}{L^2(1+\varphi_z)} & 0 & 0 & \frac{12EI_y}{L^3(1+\varphi_z)} & 0 & 0 & -\frac{6EI_y}{L^2(1+\varphi_z)} \\
0 & 0 & 0 & -\frac{GJ}{L} & 0 & 0 & 0 & 0 & 0 & \frac{GJ}{L} & 0 & 0 \\
0 & \frac{6EI_z}{L^2(1+\varphi_y)} & 0 & 0 & \frac{(2-\varphi_y)EI_z}{L(1+\varphi_y)} & 0 & 0 & -\frac{6EI_z}{L^2(1+\varphi_y)} & 0 & 0 & \frac{(4+\varphi_y)EI_z}{L(1+\varphi_y)} & 0 \\
0 & 0 & \frac{6EI_y}{L^2(1+\varphi_z)} & 0 & 0 & \frac{(2-\varphi_z)EI_y}{L(1+\varphi_z)} & 0 & 0 & -\frac{6EI_y}{L^2(1+\varphi_z)} & 0 & 0 & \frac{(4+\varphi_z)EI_y}{L(1+\varphi_z)}
\end{bmatrix} \quad (2)$$

Where $\Phi_z = 12EI_y/(k_sAGL^2)$, $\Phi_y = 12EI_z/(k_sAGL^2)$, $J = t^4/3$ for the square cross section and k_s = 5/6.

Since $[\mathrm{K}]^e$ is based on the local coordinate system (*xoy*) as shown in Fig.1, and for cellular structures individual struts are likely orientated differently, additional transformation is needed to convert the stiffness matrix into the more consistent global coordinate system ($\bar{x}o\bar{y}$) by using the transformation matrix $[T]^e$. The matrix $[T]^e$ is applicable to the transformation of forces and displacements between the two coordinate systems. Apply such transformation to the applied forces and the displacements, and the stiffness matrix under global coordinate system $[\bar{K}]$ can be expressed as

$$[\bar{K}] = [T]^{eT} \cdot [K]^e \cdot [T]^e. \quad (3)$$

By using Equation (3), the element stiffness matrices of each strut can be obtained. Then one can simply combine all of these element stiffness matrices $[\bar{\mathrm{K}}]$ together to get the global stiffness matrix [K] for the entire structure. Then the problem becomes

$$[F] = [\mathrm{K}][\mathrm{d}] \quad (4)$$

To obtain the nodal displacements, Equation (4) needs to be solved. However, the solution of Equation (4) is not unique, because the structure has not been adequately restrained. It is noted that the 3D lattice structures are usually subjected to the loading conditions that are applied on the boundaries, and there does not exist external forces at the internal nodes. This means that on the boundaries most of the displacements can be considered as either zero (fully constrained) or known values, and the external forces are always zero at the internal nodes. Therefore, the displacements $[d]$ and forces $[F]$ can be reorganized into the known part and

unknown part for further calculation. Therefore, the Equation (4) can be rewritten as

$$\begin{bmatrix} A_{11} & A_{12} \\ A_{21} & A_{22} \end{bmatrix} \begin{bmatrix} d_{unknown} \\ d_{known} \end{bmatrix} = \begin{bmatrix} F_{known} \\ F_{unknown} \end{bmatrix} \tag{5}$$

where $d_{unknown}$ is the vector of unknown displacements, d_{known} is the vector of known displacements, F_{known} is a vector of known forces and $F_{unknown}$ is a vector of unknown forces. From Equation (5), the unknown displacements can be solved as

$$d_{unknown} = {A_{11}}^{-1}(F_{known} - A_{12}d_{unknown}). \tag{6}$$

Therefore, with the knowledge of d_{known}, all the displacement components can be determined for the calculation of the internal forces for each strut. Furthermore, the stress distribution of every strut can be established from the results of the nodal displacements.

3.2 Initial and progressive failure process modelling

Within the scope of this paper, the initial failure in the lattice structures was set to occurs at the strut with the maximum stress. Upon initial failure, the failed strut is no longer contributing to the load bearing of the structures, and the stresses in the remaining lattice struture would be redistributed. Further increments in the applied loading or displacement will result in failure of other struts within the structure. This progressive failure process continues until complete failure (the structure fracture into two parts) of the whole structure occurs. Such failure mode is gauranteed as in this study only tensile failure was considered. Besides, the maximum principal stress is used as the failure criteria for the determination of the progressive failure process of the cellular structures. The initial failure started at the strut with the maximum principal stress. This was achieved by stress analysis with individual beams once the force components are determined from Equation (6). The principal stress of individual beams is determined by both the normal stresses and shear stress. The normal stress is contributed by both the bending moment and axial force, while the shear stress is contributed by the shear force. When the principal stress of one strut reaches the yield strength of the material, the corresponding strut will fracture, which forms the initial failure. After the initial failure, the fractured strut was removed from the lattice structures, and the stress status of the remaining structures was re-calculated. Such iterative calculations were utlized to determine the sequence of the strut fracture.

4. Results and discussion

The tensile process of the four types cellular structures were numerically simulated through the above introduced methods. The effect of the unit cell numbers on the tensile failure patterns, the tensile strength, the modulus and energy absorption were analyzed.

4.1 Tensile failure responses of four structures

To investigate the effect of the unit cell numbers of the structure on the tensile response, the strain-stress responses of all the four structures were analyzed, shown in Fig.3. In Fig. 3, the x-axis and y-axis of each curve indicate the strain and stress respectively. For all the four structures, the strain-stress curves of the strut failure exhibit the perfect elastic-brittle failure characteristics typical to the brittle materials with maximum stress failure mode that was adopted in this study. For the BCC, octahedral and octet-truss structures, the strain-stress curves exhibit some obvious saw tooth-like patterns, with critical stress levels decrease. For the auxetic structure, the strain-stress curves just exhibit a single stress peak, which indicate a catastrophic failure.

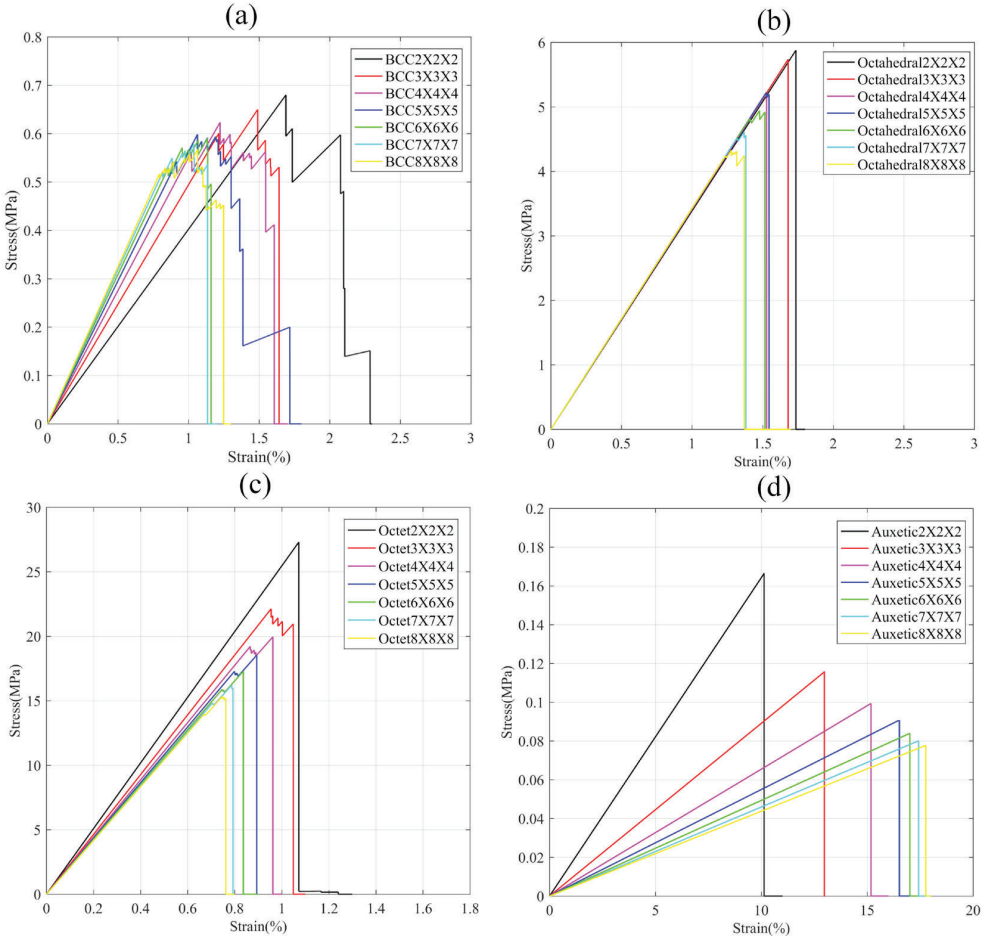

Fig. 3 The strain-stress curves of four structures with different unit cell numbers: (a) BCC; (b) Octahedral; (c) Octet-truss; (d) Auxetic

It is worth noting that even though the BCC, octahedral and octet-truss structures exhibit the saw tooth-like strain-stress curves, the distribution and the value of these stress peaks are significantly different. For the BCC structures shown in Fig.3 (a), the stress peaks distribute more uniformly from the first fracture unit the total failure of the structure. For the octahedral shown in Fig.3 (b) and octet-truss shown in Fig. 3(c), the distribution of their stress peaks is more concentrated. And stress values of these peaks are more close to the first peak. From the corresponding strains of these peaks, we can also see that the fracture process of these three

structures is a progressive fracture evolution which is similar to the crack propagation. Among these three structures, the BCC structure shows a relatively stable and slow crack propagation compared with the octahedral and octet-truss structures. For the auxetic structures shown in Fig. 3(d), the fracture pattern is more catastrophic, the whole structure fails right after the fracture initiates.

4.2 Tensile strength, Young's modulus and energy absorption analysis of four structures

The effect of the unit cell numbers on the normalized tensile strength (the tensile strength divided by the relative density) was shown in Fig. 4(a). From Fig. 4(a), it can be seen that the normalized tensile strength of all the four structures decreased when the unit cell numbers increased. The octahedral and octet-truss structures exhibited much higher normalized tensile strengths than that of the auxetic and BCC structures. Besides, both the BCC and the auxetic structures exhibit relatively consistent strength levels with varying unit cell numbers, in comparison with the other two types of structures. Such observation also contradicts with the previous suggestion of the size effects with these structures, in which the size effects appear to converge when the vertical (i.e. along the loading direction) numbers of unit cells are identical to the lateral number of unit cells [10]. While additional investigation of this subject is required, it was speculated that the discrepancies could be at least partly attributed to the different methods utilized for the calculations and the different geometrical parameter settings for the cellular designs.

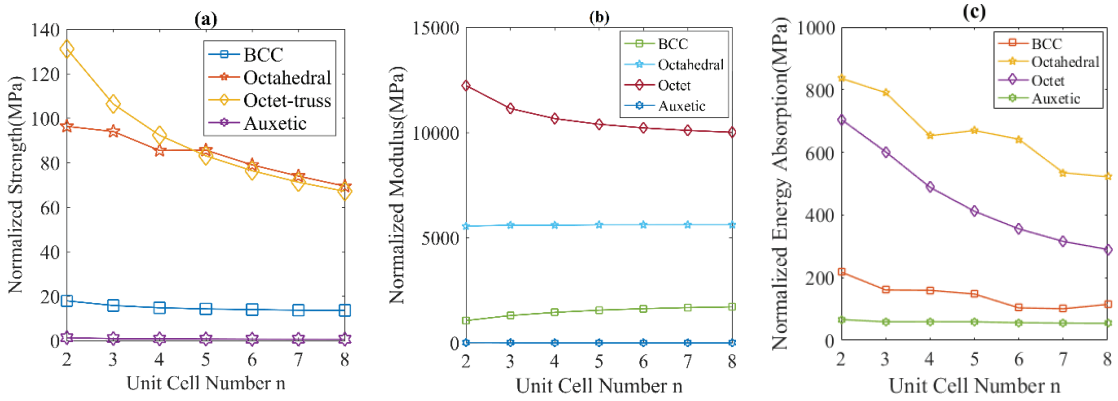

Fig. 4 Size effects on the normalized tensile strength (a), normalized Young's modulus (b) and normalized energy absorption (c) of four structures

The effect of the unit cell numbers on the normalized Young's modulus (the Young's modulus divided by the relative density) was shown in Fig. 4(b). The octet-truss structures exhibits the highest modulus at all unit cell number range, while the auxetic structures exhibit the lowest. For the octet-truss structures, he normalized Young's modulus also exhibit most significant decreasing trend when the unit cell numbers increase. On the other hand, for the other types of structures, the trends appear much less significant.

The effect of the unit cell numbers on the normalized energy absorption (the energy absorption divided by the relative density) was shown in Fig. 4(c). For perfectly elastic

materials, the energy absorption is determined by both the maximum strength and the elastic modulus. From the results, the normalized energy absorptions of all the structures decreased when the unit cell number increased, which agree with the trends observed from the normalized elastic modulus and strength. For the auxetic structures, it is expected that the size effect is minimized, and therefore the energy absorption characteristics should also exhibit minimum size effects. On the other hand, with the other structures, the size effects are introduced either through reduced elastic modulus or reduced maximum strength.

4.3 Tensile failure pattern of four structures

Using the proposed fracture model, the predicted tensile failure patterns of four structures are shown in Fig. 5 to Fig. 8 respectively. Fig. 5 shows the tensile failure patterns of the BCC structures. From Fig. 5, the BCC structures exhibit a diagonal or V shape fracture patterns when the unit cell numbers are smaller than 8x8x8. When the unit cell numbers increase beyond 8, the fracture patterns exhibit another consistent fracture pattern located in the middle. Combining the strain-stress curves shown in Fig. 3(a), it is seen that the structures undergo more fracture progression steps (more stress peaks in the strain-stress curves indicate more fracture steps) before the total failure of the structure. In addition, for the BCC structures with larger unit cell numbers, prior to the occurrence of the primary fracture path located in the middle layer, some of the struts located in the corner would crack first.

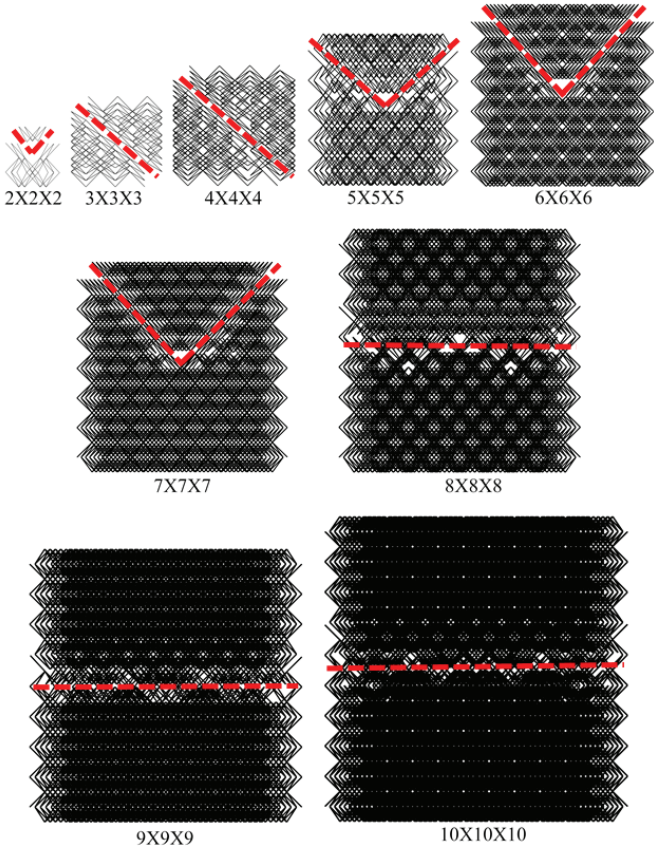

Fig. 5 Fracture patterns of BCC structures with different unit cell numbers

Fig. 6 shows the tensile failure patterns of the octahedral structures. When the unit cell numbers are smaller than 6x6x6, the fracture path was located in the middle layer of the structures. When the unit cell numbers are larger than 5x5x5, the fracture exhibited a more tortuous pathway that transitions from the corner to the middle. And also from Fig. 3(b), for the structures with smaller unit cell numbers, the fracture tend to be more catastrophic. When the fracture starts, the structure fails immediately. In contrast, for the structures with larger unit cell numbers, the fracture tends to have more steps. The structures can retain most of the overall strength after some early crack steps. This might provide a potentially useful design guideline for choosing the unit cell numbers for the design of fracture toughness of the BCC structures.

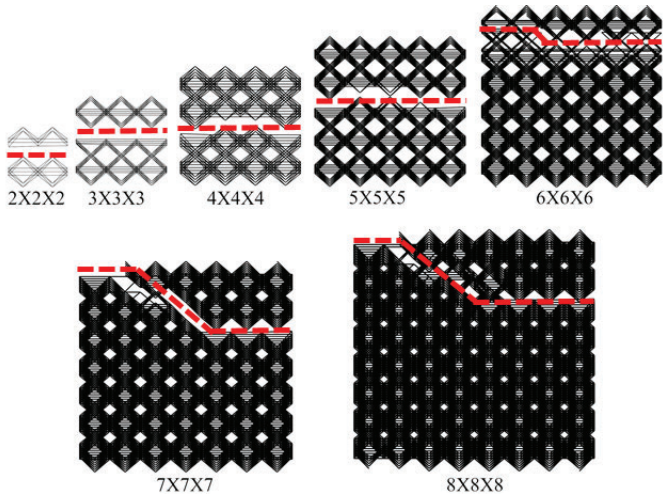

Fig. 6 Fracture patterns of octahedral structures with different unit cell numbers

Fig. 7 shows the tensile failure patterns of the octet-truss structures. The fracture patterns are relatively consistent with different unit cell numbers. The fracture initiates at the corner of the structures, and then propagates towards the middle region of the structures. From Fig. 3(c), it is seen that the octet-truss structures have a similar crack propagation process with the octahedral structures. The structures with larger unit cell numbers tend to exhibit more stable crack propagation process before the total failure of the structures.

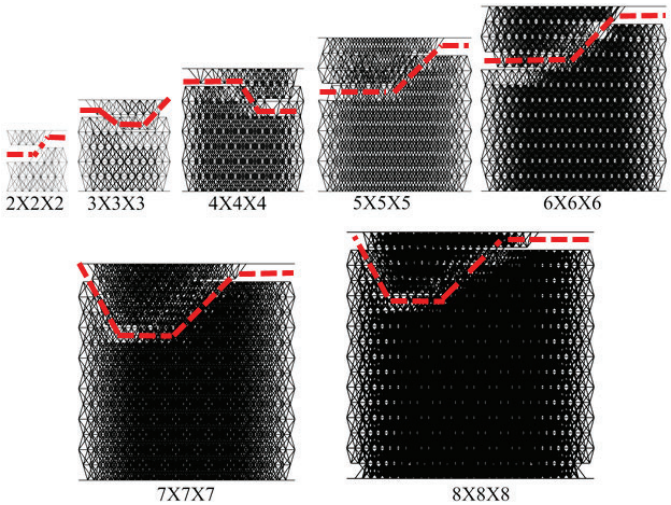

Fig. 7 Fracture patterns of octet-truss structures with different unit cell numbers

Fig. 8 shows the tensile failure patterns of the auxetic structures. The fracture patterns are highly consistent across different unit cell numbers. For the structures with smaller unit cell numbers, the fractures locate at the boundary layers. For the structures with larger unit cell numbers, the fractures occur at the second layers. From the Fig. 3(d), it is seen that the strain-stress curves have only one stress peaks, which indicates that the structure will fail immediately and lose all the loading capacity once the fracture starts. Such distinct "layerwise" fracture pattern was also experimentally observed in previous literature, although it is also speculated that such behavior might be specific to certain geometry design parameter ranges [11].

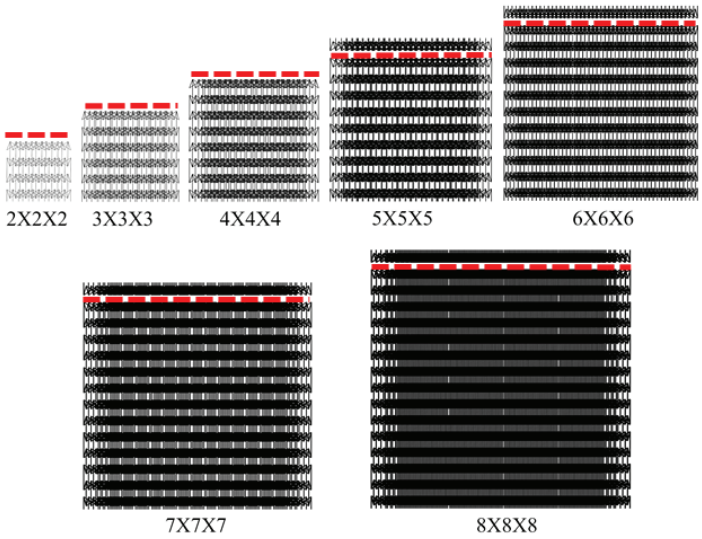

Fig. 8 Fracture patterns of auxetic structures with different unit cell numbers

5. Conclusions

In this paper, the uniaxial tensile failure characteristics of four types of cellular structures with different unit cell numbers were analyzed based on an analytical model using the matrix displacement method. The differences in the fracture modes of four types cellular structures and the evolution processes were investigated. The findings presented in this study are summarized below:

1. The type of unit cell topology has significant effect on the fracture mode of the lattice structure. The fracture process of the BCC structure tends to be a progressive fracture evolution, while for the octahedral and octet-truss structures, the fracture process experiences less fracture stages compared with the BCC structures. The auxetic structure appears to exhibit rather catastrophic fracture failure.

2. For the fracture evolution process, the BCC, octahedral and octet-truss structures can hold most of the loading capacity once the fracture begins. While for the auxetic structure, the whole structure will lose the loading capacity once the fracture occurs.

3. The size effect analysis showed that the tensile failure behavior tends to converge to

consistent patterns when the unit cell numbers increase sufficiently, even though different structures may have different characteristic stabilization unit cell numbers.

It is also worth noting that the geometry parameters of the unit cell designs were randomly chosen in this study, whereas various works have clearly suggested that specific geometry parameter setting could also potentially have significant impact on the overall performance to the structures. Therefore, while the insights from this study could be helpful towards further understanding of the design characteristics of the cellular structures, more systematic studies would benefit a comprehensive view of the problem.

Reference

[1] Heinl, P., Müller, L., Körner, C., Singer, R. F., & Müller, F. A. (2008). Cellular Ti–6Al–4V structures with interconnected macro porosity for bone implants fabricated by selective electron beam melting. Acta biomaterialia, 4(5), 1536-1544.

[2] Montillet, A., Comiti, J., & Legrand, J. (1993). Application of metallic foams in electrochemical reactors of filter-press type Part I: Flow characterization. Journal of applied electrochemistry, 23(10), 1045-1050.

[3] Boomsma, K., Poulikakos, D., & Zwick, F. (2003). Metal foams as compact high performance heat exchangers. Mechanics of materials, 35(12), 1161-1176.

[4] Lu, T. J., Stone, H. A., & Ashby, M. F. (1998). Heat transfer in open-cell metal foams. Acta materialia, 46(10), 3619-3635.

[5] Simone, A. E., & Gibson, L. J. (1998). Effects of solid distribution on the stiffness and strength of metallic foams. Acta Materialia, 46(6), 2139-2150.

[6] Jin, I., Kenny, L. D., & Sang, H. (1990). U.S. Patent No. 4,973,358. Washington, DC: U.S. Patent and Trademark Office.

[7] Ozdemir, Z., Hernandez-Nava, E., Tyas, A., Warren, J. A., Fay, S. D., Goodall, R., Todd, I., & Askes, H. (2016). Energy absorption in lattice structures in dynamics: Experiments. International Journal of Impact Engineering, 89, 49-61.

[8] Ozdemir, Z., Tyas, A., Goodall, R., & Askes, H. (2017). Energy absorption in lattice structures in dynamics: Nonlinear FE simulations. International Journal of Impact Engineering, 102, 1-15.

[9] Li, P., Wang, Z., Petrinic, N., & Siviour, C. R. (2014). Deformation behaviour of stainless steel microlattice structures by selective laser melting. Materials Science and Engineering: A, 614, 116-121.

[10] Yang, L. (2016). A study about size effects of 3D periodic cellular structures. In Proceedings of the 27th International Solid Freeform Fabrication (SFF) Symposium, Austin, TX.

[11] Yang, L., Harrysson, O., West, H., & Cormier, D. (2012). Compressive properties of Ti–6Al–4V auxetic mesh structures made by electron beam melting. Acta Materialia, 60(8), 3370-3379.